An experimental investigation on the discrete Poisson's upward continuation of anomalous gravity field data

MEHMET SİMAV
msimav@msu.edu.tr

BİHTER EROL
bihter@itu.edu.tr

MUHAMMET AKİF GÜLENDER
muhammetakif.gulender@harita.gov.tr

SERDAR EROL
erol@itu.edu.tr

Follow this and additional works at: https://journals.tubitak.gov.tr/earth

Part of the Earth Sciences Commons

Recommended Citation

An experimental investigation on the discrete Poisson's upward continuation of anomalous gravity field data

Mehmet SİMAV[1,*] ![ID] , Bihter EROL[2] ![ID], Muhammet Akif GÜLENDER[3] ![ID], Serdar EROL[2] ![ID]

[1]Rectorate of National Defence University, İstanbul, Turkiye
[2]Department of Geomatics Engineering, Faculty of Civil Engineering, İstanbul Technical University, İstanbul, Turkiye
[3]General Directorate of Mapping, Ankara, Turkiye

Abstract: The Poisson upward continuation of gravity field functionals, typically given on the Earth's irregular topography with limited spatial extent, necessitates some proper treatments due to the theoretical requirements. This study reviews the Poisson theory and investigates a more rigorous methodology for the numerical solution of the spherical integral equation by addressing many issues such as spherical-Earth model implementation, far-zone effect, Poisson kernel modification, and suitable ground data reduction scheme. We first explore the far-zone effect and search for an optimal near-zone spherical cap radius above which the truncation error is negligible. We then compare different variants of remove-restore technique with a modified Poisson kernel to upwardly continue the ground gravity field data to predefined height levels close to the Earth's surface. Different combinations of long- and short-wavelength contributions are studied extensively. Numerical experiments have been performed using simulated ground gravity anomaly and gravity disturbance data synthesized from ultrahigh-degree global geopotential model (GGM). Numerical results show that the far-zone contribution may reach up to several milligal levels and should be taken into consideration when the cap size radius is less than 1° for the upward continuation height levels between 3000 m and 5000 m above the sea level. Among the various solutions, the best agreement between the Poisson upward-continued ground data and its synthetic counterpart has been obtained when the gravity field data input directly into the Poisson integral is reduced both for GGM and residual terrain model (RTM).

Key words: Upward continuation, spherical Poisson integral, kernel modification, ground gravity anomaly, far-zone effect, remove-restore

1. Introduction

Recent advances in many engineering fields have enabled geoscientists to measure the Earth's gravity field with unprecedented accuracy from crust to exosphere using modern instruments such as ocean floor, borehole, shipborne, land, airborne and satellite gravimeters (Smith, 1950; Jageler, 1976; Torge, 1989; Sasagawa et al., 2003; Hinze et al., 2013; Sandwell et al., 2014; Vaníček and Kingdon, 2015). Because the gravity information is generally not required at the measurement locations in most phases of the data processing, upward or downward continuation is applied to compute corresponding gravity values at different height levels in order to compare or merge distinct types of gravimetry data or to smooth/enhance the regional gravity field (Courtillot et al.,1978; Blakely, 1995, Fedi et al., 1999; Kern, 2003).

There are various deterministic and stochastic numerical approaches in the literature to upward/downward continue or combine heterogeneous potential field data at varied height levels, such as least-squares collocation (Hwang et al., 2007; Yildiz et al., 2017; Simav et al., 2020; Willberg et al., 2020), least-squares spectral combination (Sjöberg, 1981; van Gelderen and Rummel, 2001; Kern et al., 2003), spherical harmonic analysis (Smith et al., 2013; Qu et al., 2021), radial basis functions (Li et al., 2022), analytical upward/downward continuation (Moritz, 1980; Huang, 2002), and Poisson's integral methods (Cruz and Laskowski, 1984; Novák and Heck, 2002; Alberts and Klees, 2004; Guo and Tao, 2020).

Continuation problem is the solution of the well-known first boundary value problem of the potential theory, named also Dirichlet's problem, which simply takes the Earth's gravity field data on the boundary surface as input and predicts the corresponding values outside the surface. If the shape of a boundary is a spherical surface, then the Dirichlet's problem can be solved by means of spherical harmonics. Alternatively, an explicit solution of Dirichlet's problem for the exterior of the sphere can be expressed in terms of Poisson's integral. Given a harmonic function $V(R, \Omega') = V(R, \varphi', \lambda')$ on the surface of a

* Correspondence: msimav@msu.edu.tr

geocentric sphere with radius R, the values of the function outside the sphere $V(r, \Omega) = V(r, \varphi, \lambda)$ can be computed by Poisson's upward continuation integral formula as follows with an abbreviation $\int_{\Omega'} d\Omega'$ representing the integration over the whole sphere (Heiskanen and Moritz, 1967)

$$V(r, \Omega) = \frac{1}{4\pi} \int_{\Omega'} K(r, \psi, R) V(R, \Omega') d\Omega' = \frac{1}{4\pi}$$

$$\int_{\varphi'=-\pi/2}^{\pi/2} \int_{\lambda'=0}^{2\pi} K(r, \psi, R) V(R, \Omega') \cos\varphi' d\varphi' d\lambda' \qquad (1)$$

where Ω and Ω' are the solid angles denoting the spherical latitudes and longitudes of computation (φ, λ) and integration points (φ', λ'), respectively. r is the geocentric radius of the computation point outside the sphere, i.e., $r \geq R$. The well-known Poisson kernel function $K(r, \psi, R)$ is expressed as (Heiskanen and Moritz, 1967):

$$K(r, \psi, R) = \frac{R(r^2 - R^2)}{L^3} \qquad (2)$$

where L and ψ are the Euclidean and angular distances, respectively, between a computation point outside the sphere and integration point on the sphere.

When the function is known above the surface and its corresponding values on the sphere are sought, we face the problem of inverse Poisson or Poisson's downward continuation. By definition, upward continuation behaves like a low-pass filter and tends to smooth the details of potential field data. In exploration geophysics, this transformation reduces the effect of shallow bodies and accentuates anomalies caused by deep sources. On the other hand, downward continuation clearly amplifies the shortest wavelengths of measured data. It enhances small-scale sources and improves their spatial resolutions. From computational point of view, the Poisson's upward continuation is a direct or forward problem in contrast to Poisson's downward continuation, which is one of the ill-posed inverse problems of potential theory whose solution may not be unique and stable (Courtillot et al., 1978; Schwartz, 1978; Blakely, 1995).

While the basic theory behind Poisson's upward continuation is relatively simple and straightforward compared to the downward continuation procedure, there are some issues that need be considered in implementing the integral formula. According to Eq. (1), potential field data, e.g., gravity anomaly or gravity disturbance, should be given on the level surface of a geocentric sphere and integration should be extended over the entire globe. However, gravity measurements are typically performed on the undulating surface of Earth's visible and irregular topography. Moreover, gravity measurements are often limited in their spatial extent and not continuously provided over the entire Earth. Therefore, some assumptions and approximations have to be applied for the practical implementation of Poisson's upward continuation.

In most geoscience applications regarding the potential field continuation, the field data given on an undulating surface are first preprocessed to somehow meet the horizontal level surface condition. The preprocessing methods include smoothing, filtering or detrending in frequency or spatial domains. Moreover, the anomalous data are usually reduced for high-frequency topographic variations by simple or refined Bouguer correction since it is distorted by the surrounding terrain. Afterward, the Poisson upward continuation formula is applied using filtered and/or reduced data, generally relying on flat-Earth or planar approximation in space domain, as well as in spectral domain based on Fourier techniques (Schwarz et al., 1990; Forsberg, 1998). The far-zone contribution or truncation error is mostly ignored, at least for local and regional studies (Guo and Tao, 2020).

In this study, point-to-point discrete Poisson's upward continuation of ground data has been revisited to investigate a more rigorous methodology for the numerical solution of the spherical integral equation by addressing spherical-Earth model implementation, far-zone effect, Poisson kernel modification, and suitable ground data reduction scheme. Discretization of the integral formula in the near-zone, far-zone contribution and kernel modification, remove-restore procedure, i.e., reducing the ground gravity field data of the long- and high-frequency gravity field variations using global geopotential and digital elevation models has been reviewed. Different combinations of long- and short-wavelength contributions are studied extensively. Three topographic reduction techniques, i.e., spherical Bouguer, residual terrain model (RTM), and Helmert's second method of condensation, are applied to model the short-wavelength topographic gravity effects. Synthetic grid data with a resolution of 1' × 1' at various height levels close to the Earth's surface are generated from an ultrahigh-resolution global geopotential model (GGM) complete to degree and order (d/o) 5540 within a test region covering one of the roughest parts of Türkiye. The upward-continued synthetic ground gravity field data are compared to the spherical harmonic model to identify the best discretization methodology and to assess the performance of kernel modification. Some freely available computer programs are developed for the evaluation of the abovementioned computations. Section two of the manuscript reviews the methodology and presents the expressions for point-to-point discrete spherical Poisson's upward continuation of ground gravity anomalies and disturbances. Section three describes the study region and

explains the data used in the numerical investigations. Section four presents and evaluates the results. Finally, the summary and conclusions are provided in the last section.

2. Review of the basic theory

The Poisson upward continuation integral for any harmonic function expressed in Eq. (1) is replaced by summation when it is to be discretized in practice but with two further modifications due to the lack of global data coverage. In the first modification, the integration domain is divided spatially into near- and far-zones. The near-zone is the area where local or regional data that contribute the dominant part of the integral value are available. It is routinely chosen as spherical cap with an angular radius of ψ_0. The far-zone is the region over the remainder of the sphere, merely accounting for a small part of the integration value. In the second modification, the local or regional gravity data inside the near-zone is split into low-, medium-, and high-frequency spectrum where the remove-restore step together with the Poisson kernel modification is applied.

2.1. Near-zone contribution: discrete Poisson integral

The integral equation in Eq. (1) can be rewritten for the gravity anomaly data $\Delta g(R, \Omega')$ given on a geocentric sphere and further developed for the near- and far-zone contributions as follows (Huang, 2002; Alberts and Klees, 2004; Li et al., 2022):

$$\Delta g(r, \Omega) = \frac{R}{4\pi r}$$

$$\left(\int_{\Omega_0'} K(r, \psi, R)\, \Delta g(R, \Omega') d\Omega' + \int_{\Omega' - \Omega_0'} K(r, \psi, R)\, \Delta g(R, \Omega') d\Omega' \right) \quad (3)$$

where Ω_0' and $\Omega' - \Omega_0'$ represents the near- and far-zone regions, respectively. The same equation is also valid for the gravity disturbance δg by altering the terms $\Delta g(R, \Omega')$ and $\Delta g(r, \Omega)$ with $\delta g(R, \Omega')$ and $\delta g(r, \Omega)$, respectively. For brevity, equations will only be provided for the gravity anomaly hereinafter, as the formulas for gravity disturbance are analogous. The first integration on the right-hand side of Eq. (3) is the near-zone contribution where the Poisson upward continuation integral is applied. The integral equation has no analytical solution; therefore, numerical evaluation of the upward continuation requires the discretization of the problem.

Given angular grid of points at the surface of a geocentric sphere and the near-zone cap size ψ_0, it remains to evaluate the system of linear equations.

$$\Delta g(r_i, \Omega_i) = \sum_{j=1}^{M} B_{ij}\, \Delta g(R, \Omega_j') \quad \begin{array}{l} (i = 1, 2, \cdots, N) \\ (j = 1, 2, \cdots, M) \end{array} \quad (4)$$

where the entries of the matrix B are explicitly derived in Martinec (1996). However, for completeness, it is given in the below equation. While the upper limit of the summation M represents the total number of roving points within the near-zone, N stands for the number of computation points.

$$(5)\, B_{ij} = \begin{cases} \frac{R}{4\pi r_i} K(r_i, \psi_{ij}, R) \cos \varphi_j \Delta\varphi \Delta\lambda & \text{if } \psi_{ij} \leq \psi_0 \text{ and } i \neq j \\[2ex] \frac{R}{r_i} d^l(r_i, \psi_0, R) - \sum_{j=1, j \neq i}^{M} B_{ij} & \text{if } \psi_{ij} \leq \psi_0 \text{ and } i = j \\[2ex] 0 & \text{if } \psi_{ij} > \psi_0 \end{cases}$$

$$d^l(r_i, \psi_0, R) = \frac{1}{2} \left[\frac{r_i + R}{r_i} \left(1 - \frac{r_i - R}{L(r_i, \psi_0, R)} \right) \right] \quad (6)$$

2.2. Far-zone contribution: truncation error

The second integration on the right-hand side of Eq. (3) is the far-zone contribution also called truncation error that will be hereinafter referred to as $F_{\Delta g}(r, \Omega)$. The far-zone contribution can be evaluated from a GGM using the harmonic expansion technique given below (Huang, 2002):

$$F_{\Delta g}(r, \Omega) = \frac{R\gamma}{2r} \sum_{n=2}^{\infty} (n-1) Q_n(H, \psi_0) \sum_{m=-n}^{n} T_{n,m} Y_{n,m}(\Omega), \quad (7)$$

where $Y_{n,m}(\Omega)$ and $T_{n,m}$ represent the surface spherical harmonic functions and their fully normalized coefficients with even degree zonal reference values are subtracted, respectively. γ is the average value of gravity that can be computed using a simple approximation GM/R^2 where GM is the geocentric gravitational constant. The coefficients $Q_n(H, \psi_0)$ are denoted as truncation coefficients which can be written as (Heiskanen and Moritz, 1967):

$$Q_n(H, \psi_0) = \int_{\psi_0}^{\pi} K(r, \psi, R) P_n(\cos \psi) \sin \psi \, d\psi. \quad (8)$$

In the above equation, H represents the point height above the reference sphere, i.e., $H = r - R$, and P_n is the Legendre polynomial of degree n. The truncation coefficients can be computed either by a numerical integration or using some recursive algorithms (Paul, 1973).

2.3. Remove-restore and Poisson kernel modification

It has been a common practice to use a frequency division model in the gravity field modelling based on the remove-restore technique (Forsberg and Tscherning, 1981). The approach involves three consecutive steps. In the first step, i.e., the remove step, the ground gravity anomaly data are reduced by long-wavelength gravity field signal. Because the satellite gravimetry provides homogenous long-wavelength information, the low-frequency part of the gravity field data is derived from a satellite-only model. High-frequency part due to the topography and the atmospheric effects can also be removed from the

terrestrial data in this step. The remove step results in residual gravity field data, which are then input directly into the discrete Poisson integral in Eq. (4). In the second step, the residual gravity field data are upward-continued. In the final step, i.e., the restore step, the removed part is recomputed at the upward continuation level and added back to the output computed in the second step.

The residual gravity anomaly data are band-limited from the spectral point of view. However, the standard Poisson kernel in Eq. (2) contains full spectrum; therefore, it should be modified before the computation of near-zone contribution. The standard Poisson kernel can be expanded into the spherical harmonic series as follows (Heiskanen and Moritz, 1967):

$$K_l(r, \psi, R) = \sum_{n=0}^{L_S} (2n+1) \left(\frac{R}{r} \right)^{n+1} P_n(\cos \psi) \tag{9}$$

Frequency division can also be applied to the kernel function to obtain the low-frequency part K_l and the medium- to high-frequency part K_{mh}. Both kernel functions can be expressed as follows, where L_S represents the maximum degree of expansion and/or modification.

$$K(r, \psi, R) = K_l(r, \psi, R) + K_{mh}(r, \psi, R) \tag{10}$$

$$K_l(r, \psi, R) = \sum_{n=0}^{L_S} (2n+1) \left(\frac{R}{r} \right)^{n+1} P_n(\cos \psi) \tag{11}$$

$$K_{mh}(r, \psi, R) = \sum_{n=L_S+1}^{\infty} (2n+1) \left(\frac{R}{r} \right)^{n+1} P_n(\cos \psi) = K(r, \psi, R) - K_l(r, \psi, R) \tag{12}$$

The kernel function K_{mh} is called spheroidal Poisson kernel (Wong and Gore, 1969) which can act as a filter to eliminate the long-wavelength effects in the residual gravity field data. However, among various stochastic and deterministic kernel modifications proposed in the literature (Featherstone et al., 1998; Featherstone, 2003), the modified spheroidal Poisson kernel using Vaníček and Kleusberg's (1987) modification method is one of the most commonly applied in practice. It is clear from the above equations that the far-zone effect from degree $L_S + 1$ to ∞ is still missing in the solution. The modified kernel can minimize this by introducing the coefficients $t_n(H, \psi_0)$ (Vaníček et al., 1996). The modified spheroidal Poisson kernel is written as:

$$K_{mh}^{MS}(r, \psi, R) = K(r, \psi, R) - \sum_{n=0}^{L_S} \frac{2n+1}{2} t_n(H, \psi_0) P_n(\cos \psi) \tag{13}$$

where the modification coefficients $t_n(H, \psi_0)$ are obtained by minimizing Eq. (14), which can be rewritten as a system of linear equations as given in Eq. (15) (Novák et al., 2001).

$$min \left\{ \int_{\psi_0}^{\pi} [K(r, \psi, R)]^2 \sin \psi \, d\psi \right\} \tag{14}$$

$$\sum_{n=0}^{L_S} \frac{2n+1}{2} \int_{\psi=\psi_0}^{\pi} P_n(\cos \psi) P_m(\cos \psi) \sin \psi \, d\psi \ t_n(H, \psi_0) = Q_n(H, \psi_0) \tag{15}$$

The modified spheroidal Poisson kernel K_{mh}^{MS} is used in this study instead of the standard Poisson kernel K to evaluate the near-zone contribution when the long-wavelength reduction is applied (see Sections 4). The d^l function given in Eq. (6) for the standard Poisson kernel can be rewritten as follows for the modified spheroidal Poisson kernel.

$$d^{l,MS}(r_i, \psi_0, R) = \frac{1}{2} \left[\frac{r_i + R}{r_i} \left(1 - \frac{r_i - R}{L(r_i, \psi_0, R)} \right) - \frac{t_0(H, \psi_0)}{2} (1 - \cos \psi_0) + \sum_{n=1}^{l} \frac{2n+1}{2} t_n(H, \psi_0) R_n(\cos \psi_0) \right] \tag{16}$$

$$R_n(\cos \psi_0) = \frac{1}{2n+1} [P_{n+1}(\cos \psi_0) - P_{n-1}(\cos \psi_0)] \tag{17}$$

2.4. Effect of topographic masses
After removing the long-wavelength gravity field signal from the terrestrial gravity anomaly data, there remains medium- to high-frequency signals in the residual data. The high-frequency part due to the surrounding topography can also be removed from the residual data to smooth the field. The removed effects of the topographic masses are then added back at the upward continuation levels in the restore step.

Ground gravity anomalies or disturbances are given on the Earth's surface. However, the Poisson geometry requires that the data to be upward-continued refer to points on the surface of a geocentric sphere. It is a well-known fact that the difference between the undulating surface gravity anomaly and the level surface anomaly on the sphere increases as the roughness of the field increases; in other words, the rougher the field, the larger the difference. Conceptually, the ground gravity anomalies would be analytically continued to the surface of sphere to obtain level surface anomalies which requires the vertical gradients of the field. However, downward continuation of surface gravity anomalies to a level surface has some theoretical problems. The downward continuation is classified as an ill-posed problem due to the fact that a comparatively smooth function of the gravity field is utilized to obtain a more detailed and rougher function. A small high-frequency error in the input gravity field data will be amplified, which will intrinsically lead to a large output error when continued downwards. However, the problem of high-frequency irregularities in the field reduces in the case of a smooth anomaly field. If the Earth's visible topography is physically regularized in some way in which the high-frequency components of the gravity signals are smoothed and dampened by compensating the topographical masses, the field can then be upward or downward continued less problematically by the Poisson integral (Martinec, 1996).

There are several reduction techniques in the literature, each treating the topography in a different manner. They differ from each other depending on how the topographical masses outside the reference sphere are dealt with (Tziavos

and Sideris, 2013). Among them, we will study the spherical Bouguer (Vaníček et al., 2004) reduction, RTM reduction (Forsberg and Tscherning 1981; Forsberg, 1984), and Helmert's second method of condensation (Vaníček and Martinec, 1994).

The Bouguer reduction removes all the topographic masses above the geoid or the reference sphere. On the other hand, the RTM reduction scheme introduced by Forsberg (1984) uses a mean elevation surface as a reference instead of geoid. This mean elevation can be computed by low-pass filtering the local terrain heights or from the spherical harmonic expansion of Earth's topography using the fully normalized height coefficients. The topographical masses above this mean elevation surface are removed and masses are filled up below this surface. The topographical effect on gravity at a computation point $A^t(r, \Omega)$ for both types of reduction methods can be expressed as follows with a slight change in the lower limit of the innermost integration:

$$A^t(r, \Omega) = -G \int_{\varphi'=-\pi/2}^{\pi/2} \int_{\lambda'=0}^{2\pi} \int_{r'=r_1}^{r_2}$$

$$\rho^t(\varphi', \lambda', r') \frac{\partial L^{-1}(r, \psi, r')}{\partial r} r'^2 \cos \varphi' d\varphi' d\lambda' dr' \quad (18)$$

where G is the Newton's gravitational constant and $\rho^t(\varphi', \lambda', r') = \rho^t(\Omega', r')$ is the topographic density at the integration point generally assumed to be constant $\rho^t = 2670 \text{ kgm}^{-3}$. The $\partial L^{-1}(r, \psi, r')/\partial r$ term represents the radial derivative of the reciprocal spatial distance. The lower limits of the innermost integration are equal to $r_1 = R$ and $r_1 = R + H_{ref}(\Omega')$ for the spherical Bouguer and RTM reductions, respectively. The upper limit r_2 is equal to the sum of reference sphere radius and the integration point height, i.e., $r_2 = R + H(\Omega')$ for both reduction schemes.

The volume integral in Eq. (18) can be evaluated in space domain by mass discretization using elementary geometrical bodies such as polyhedra, prisms, tesseroids and point masses (Nagy et al., 2000; Wild Pfeiffer, 2008; Tsoulis, 2012; D'Urso, 2013; Grombein et al., 2013; Uieda et al., 2016). The superposition principle can be applied to sum up the effects of all individual mass bodies. Alternatively, the triple integral can also be evaluated numerically using the quadrature methods (Novák, 2000; Simav and Yildiz, 2021).

The Helmert's second method of condensation is one of the most common gravimetric reduction schemes used in geodesy. In this scheme, the topographical masses are condensed on the geoid surface as a surface layer. The direct topographical effect (DTE) on gravity in this reduction method is computed by subtracting the attraction of condensed topographical masses $A^{ct}(r, \Omega)$ from the attraction of spherical topographical shell $A^t(r, \Omega)$ (Vaníček and Martinec, 1994) as follows:

$$DTE(r, \Omega) = A^t(r, \Omega) - A^{ct}(r, \Omega) \quad (19)$$

$$A^{ct}(r, \Omega) = GR^2 \int_{\varphi'=-\pi/2}^{\pi/2} \int_{\lambda'=0}^{2\pi} \sigma^t(\varphi', \lambda') \frac{\partial L^{-1}(r, \psi, R)}{\partial r} \cos \varphi' d\varphi' d\lambda' \quad (20)$$

The $\sigma^t(\varphi', \lambda')$ term in the above equations represents the surface density of the topographical condensation layer. It should be noted that the attraction of spherical topographical shell $A^t(r, \Omega)$ is a volume integral, whereas its corresponding condensed version $A^{ct}(r, \Omega)$ is a surface integral.

3. Study area and data description

Numerical investigations have been carried out in a test region on the southwestern coast of Türkiye bounded by a quadrangle area between 36°N–37°N and 29°E–30°E. It embodies both land and sea parts containing diverse topography of hills, mountains, and low-lying deltas, as well as relatively deep-sea trench where the topographic and gravity field variations are highly complex. Figure 1 shows the surrounding topography of the study area, as well as the boundaries of computation points and the near-zone (see Section 2.1).

The ultrahigh-degree XGM2019e combined GGM represented through spherical harmonics up to d/o 5540 (Zingerle et al., 2020) has been utilized to generate synthetic grid of 1' × 1' resolution gravity anomaly and disturbance data on the geoid and Earth's surfaces as well as at four different height levels close to the Earth's surface, i.e., 3000 m, 3500 m, 4000 m, and 5000 m above sea level. While the ground gravity field data are used as inputs to discrete Poisson upward continuation computation, the gravity anomalies and disturbances at aforementioned height levels are employed to verify the performances of upward continuation results. The synthetic gravity field data on the Earth's surface and four height levels have been computed applying the standard series expansion of spherical harmonic synthesis based on the extended-range arithmetic (Bucha and Janák, 2014). Figure 2 displays the synthetic gravity anomalies on the geoid and Earth's surfaces, respectively, within the near-zone of 5° × 5° quadrangle area bounded by 34°N–39°N and 27°E–32°E. The synthetic gravity anomalies of the computation points at the four height levels are shown in Figure 3. The descriptive statistics of the synthetic gravity anomaly (Δg) and gravity disturbance (δg) data distributed at a constant spacing of 1' × 1' within the computation and near-zone areas are presented in Table 1.

One of the latest releases of satellite-only GGM, namely GOCO06s (Kvas et al. 2021), has been used in the remove-restore procedure to reduce the long-wavelength gravity field signal and to evaluate the far-zone contribution of Poisson's upward continuation (see Section 2.2). Both combined and satellite-only GGMs can be obtained from the International Centre for Global Earth Models (ICGEM) website at http://icgem.gfz-potsdam.de.
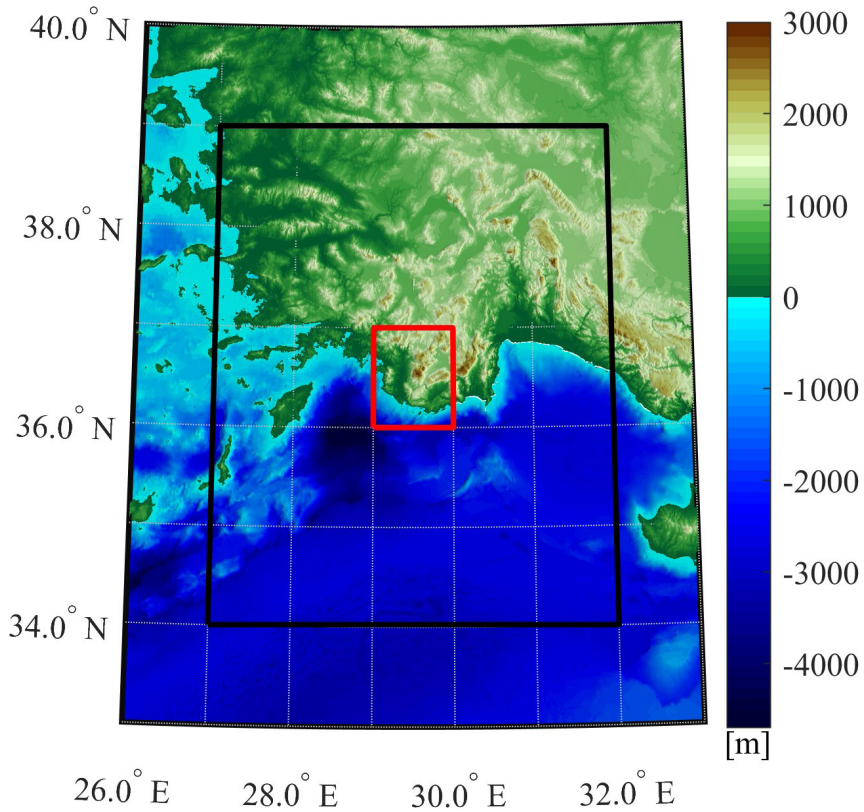
Figure 1. Topography of the study area. While the red quadrangle bounded by 36°N–37°N and 29°E-30°E represents the computation area, the black quadrangle bounded by 34°N–39°N and 27°E–32°E covers the near-zone.
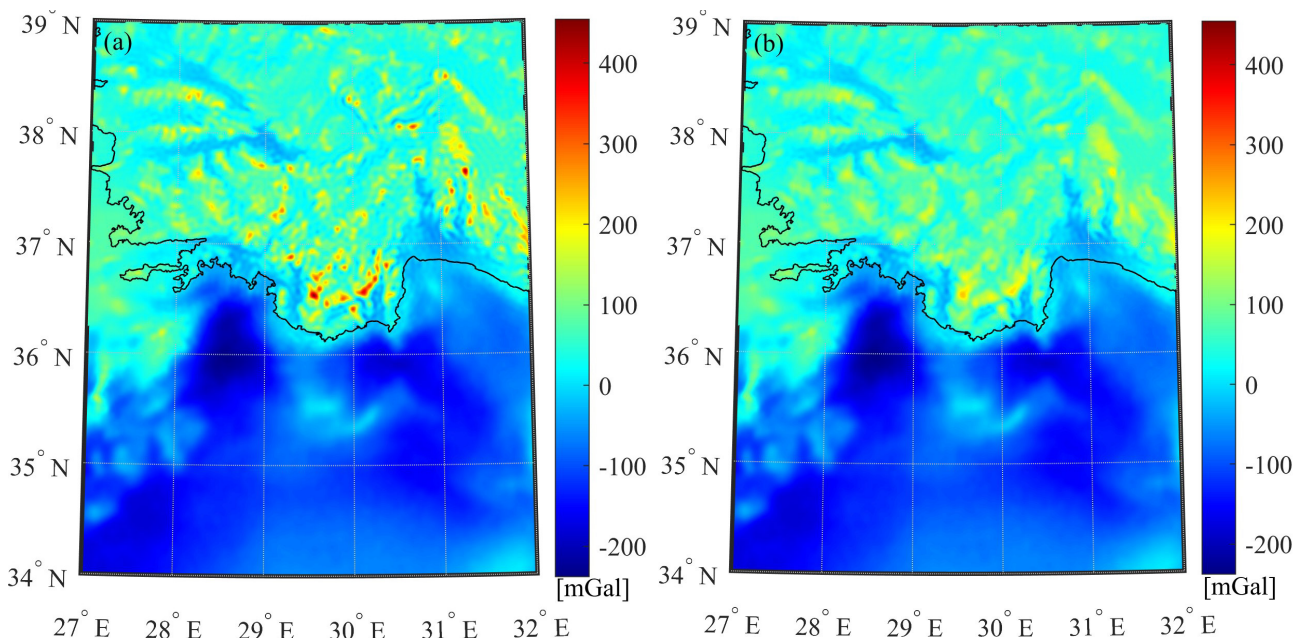
Figure 2. The synthetic gravity anomalies within the near-zone derived from xGM2019e ultrahigh-resolution GGM (a) on the geoid surface, (b) on the Earth's surface. Units are in mGal.
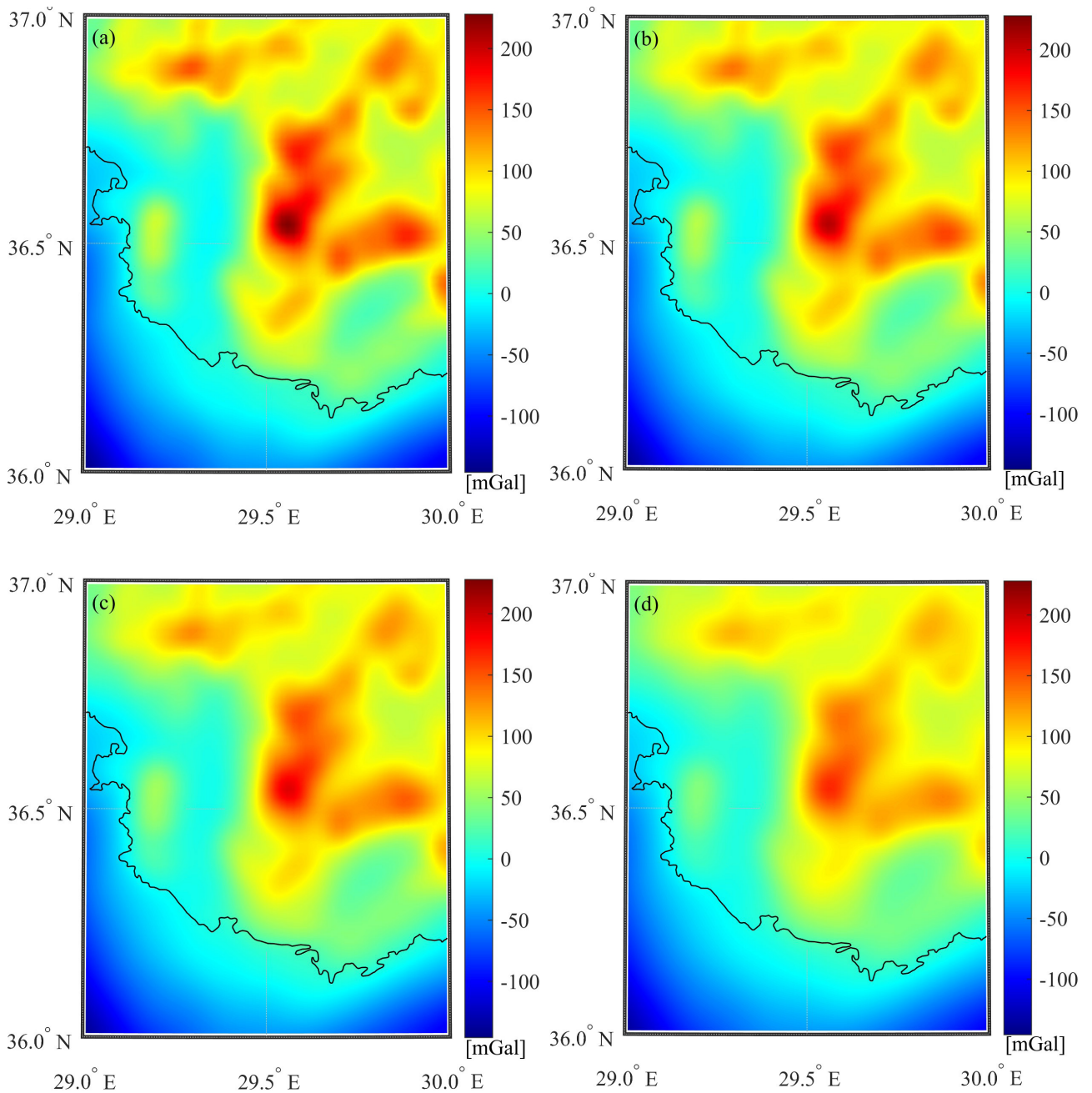
Figure 3. The synthetic gravity anomalies at four exterior height levels close to the Earth's surface. (a) 3000 m above the geoid, (b) 3500 m above the geoid, (c) 4000 m above the geoid, (d) 5000 m above the geoid. Units are in mGal.

We exploit three freely available terrain data throughout the study to determine the heights of ground points above the sea level within the study area and to evaluate the terrain gravity effects (see Section 2.4). The high-resolution multi-error-removed improved terrain digital elevation model (MERIT DEM) with spatial resolution of 3" × 3" without bathymetry information (Yamazaki et al., 2017) has been used to define ground point heights and to compute topographic effects close to these points. The second terrain data we have employed is the SRTM15+ global bathymetry and topography model (Tozer et al., 2019). While the MERIT DEM model has no global coverage and is limited to ±60° latitudes, the SRTM15+ covers the whole globe with a spatial resolution of 15" × 15". The original SRTM15+ data is resampled to 15' × 15' by box averaging method and then the resulting data is

Table 1. Descriptive statistics of the synthetic gravity anomaly (Data Type: Δg) and gravity disturbance (Data Type: δg) data distributed at constant spacing of 1' × 1' arc-min. The superscripts (1) and (2) in the first column denote the spatial extend of the data coverage. While (1) covers 5° × 5° quadrangle area bounded by 34°N–39°N and 27°E–32°E (e.g., near-zone area), (2) covers 1° × 1° quadrangle area bounded by 36°N–37°N and 29°E–30°E (e.g., computation area). Units are in mGal.

Location of gravity field data	Data type	Min	Max	Mean	Std
[1] On the geoid surface (mean sea level)	Δg	−237.36	454.12	−17.29	91.43
	δg	−234.10	462.65	−10.20	94.86
[1] On the Earth's surface (ground data)	Δg	−237.36	233.95	−18.62	87.72
	δg	−234.10	242.12	−11.54	91.22
[2] 3000 m above the geoid	Δg	−145.24	227.94	40.41	62.67
	δg	−141.24	236.17	47.80	63.86
[2] 3500 m above the geoid	Δg	−143.15	209.22	39.51	61.11
	δg	−139.12	217.41	46.90	62.31
[2] 4000 m above the geoid	Δg	−141.12	193.23	38.63	59.76
	δg	−137.08	201.38	46.01	60.96
[2] 5000 m above the geoid	Δg	−137.26	167.48	36.93	57.48
	δg	−133.17	175.58	44.29	58.69

employed to compute topographic gravity effects of the farther zone. The third terrain dataset utilized in the study is the DTM2006.0 spherical harmonic expansion of Earth's topography made available by the EGM2008 development team (Pavlis et al. 2007). It comprises fully normalized height coefficients up to d/o 2190. The DTM2006.0 model is used for the determination of reference topography to compute RTM reduction.

4. Numerical investigations

We have performed several numerical analyses on the evaluation of discrete spherical Poisson upward continuation integration in the test region. We first investigate the optimal degree of GGM and angular radius of the near-zone boundary by quantifying the maximum far-zone contribution. We then test our in-house software by continuing the gravity field data given on the geocentric sphere (~geoid surface) to four exterior height levels close to the Earth's surface and compare the results with their synthetic counterparts obtained from ultrahigh-resolution xGM2019e model. We finally study the effect of the remove-restore procedure for the continuation of the ground data which comprises the removal and restoring of: (i) long-wavelength information together with the Poisson kernel modification, (ii) long- plus the high-frequency

parts due to the topography based on spherical Bouguer reduction, (iii) long- plus the high-frequency parts based on RTM reduction, and finally (iv) long- plus the high-frequency parts based on the Helmert's second method of condensation. The flowchart of the employed reduction/restoring methodology is shown in Figure 4.

4.1. Optimal cap size determination of near-zone

It has been previously stated that the far-zone contribution or the truncation error is routinely evaluated through a GGM. Its magnitude changes depending on the spherical radius of the near-zone cap, upward continuation height level, maximum degree, and corresponding accuracy of GGM (see Section 2.2). The truncation error is small enough to be discardable provided that the cap radius is sufficiently large. However, the cap size is generally chosen to be as small as possible in practice due to the lack of available data outside the study area and to reduce the computational cost.

We determine the optimal angular radius of the near-zone experimentally by computing maximum $F_{\Delta g}(r, \Omega)$ with monotonically increasing cap radius and degree of GGM. Eight different cap radii from 0.25° to 2° with an increment of 0.25° have been tested. The spherical harmonic coefficients of GOCO06s satellite-only GGM are used up to degrees of 20, 40, 60, …, 260, 280, 300 with
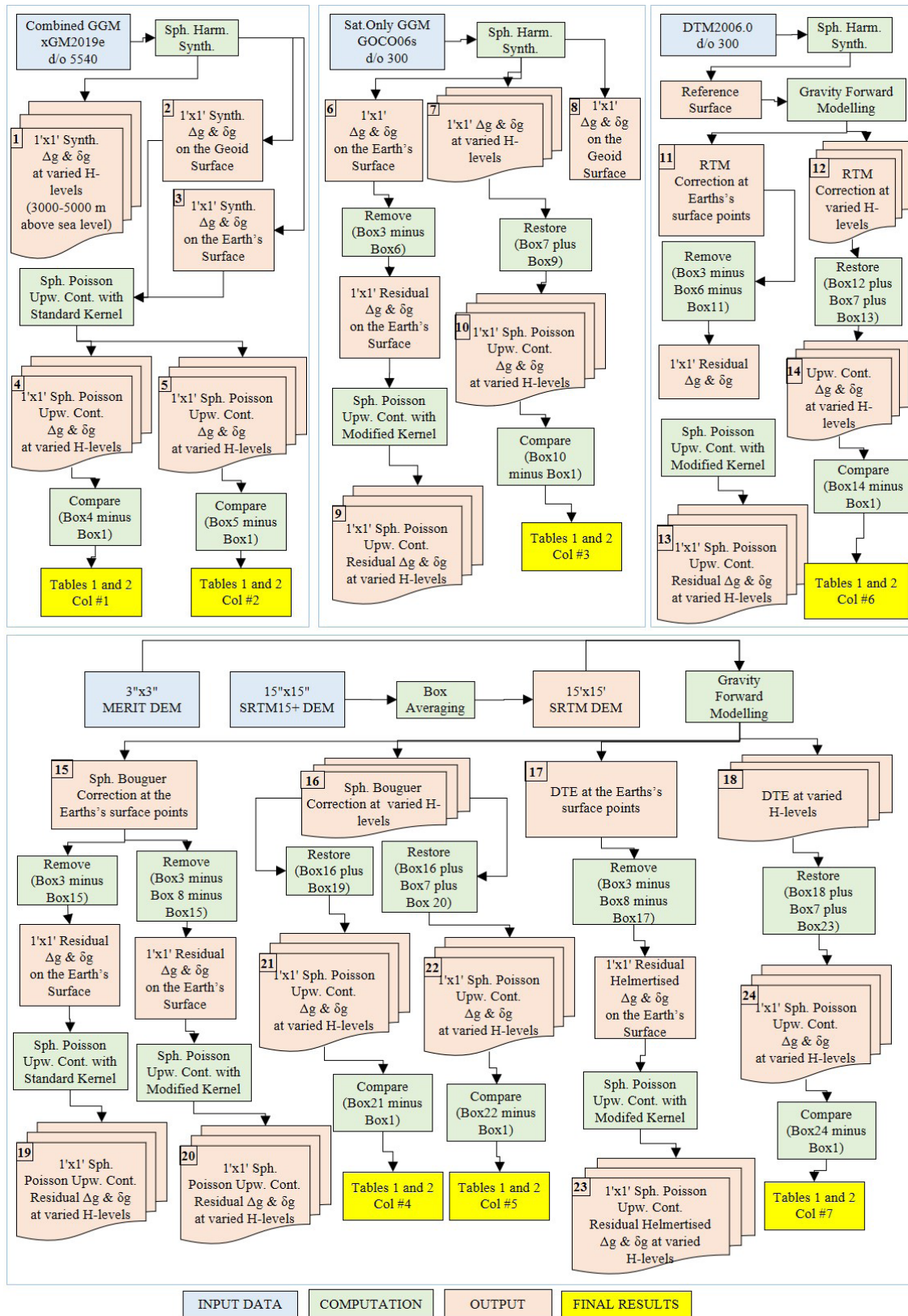
**Figure 4.** Flowchart of the remove-restore methodology.

an increment of 20. For each cap radius and maximum degree of GGM, we compute the far-zone contribution at each upward computation point at 3000 m height level above the sea level using the Eqs. (7) and (8). We then determine the maximum value of $F_{\Delta g}(r, \Omega)$ and plot its value in the corresponding color map cell (Figure 5). We perform the same computations and produce similar color maps for the other upward continuation height levels, e.g., 3500 m, 4000 m, and 5000 m.

It is clear from Figure 5 that the far-zone contribution must be taken into consideration when the cap radius is chosen less than 1° for the upward continuation height levels considered in this study. It could reach up to 12 mGal when the cap size is about 0.25° for the height level of 5000 m. Moreover, the maximum degree of the GGM should not be less than 220 for $\psi_0 = 0.25°$. It should be at least 120 for the radius of 0.50°, and at least 80 between $0.75° \leq \psi_0 \leq 1°$. The far-zone effect is negligibly small for the near-zone cap size radius of more than 1.5°. We decide to use $\psi_0 = 2°$ for our further analysis to reduce the computation time and to ignore the far-zone effect.

4.2. Upward continuation of unreduced gravity field data on the geoid and on the Earth's surfaces

The unreduced synthetic gravity anomaly and disturbance data on the geoid surface and on the Earth's topography derived from xGM2019e ultrahigh-resolution GGM within the near zone of $\psi_0 = 2°$ has been spherically upward-continued to exterior height levels based on Eqs. (4–6) to test the performance of the in-house software and to verify the Poisson's theory of the continuation.

The first data columns (#1) of Tables 2 and 3 present the descriptive statistics of the differences between the Poisson upward-continued gravity field data on the geoid surface and its synthetic counterparts for the gravity anomaly (Δg) and for the gravity disturbance (δg), respectively. It is clear that the agreement is highly satisfactory considering the commission and omission errors implied by the xGM2019e model. The standard deviation of the differences at four upward continuation height levels is around 0.05 mGal for both gravity field data with extreme values never exceeding 0.63 mGal. The comparison results can successfully prove the theoretical expression in Eq. (1) and confirms the effectiveness of the in-house software.
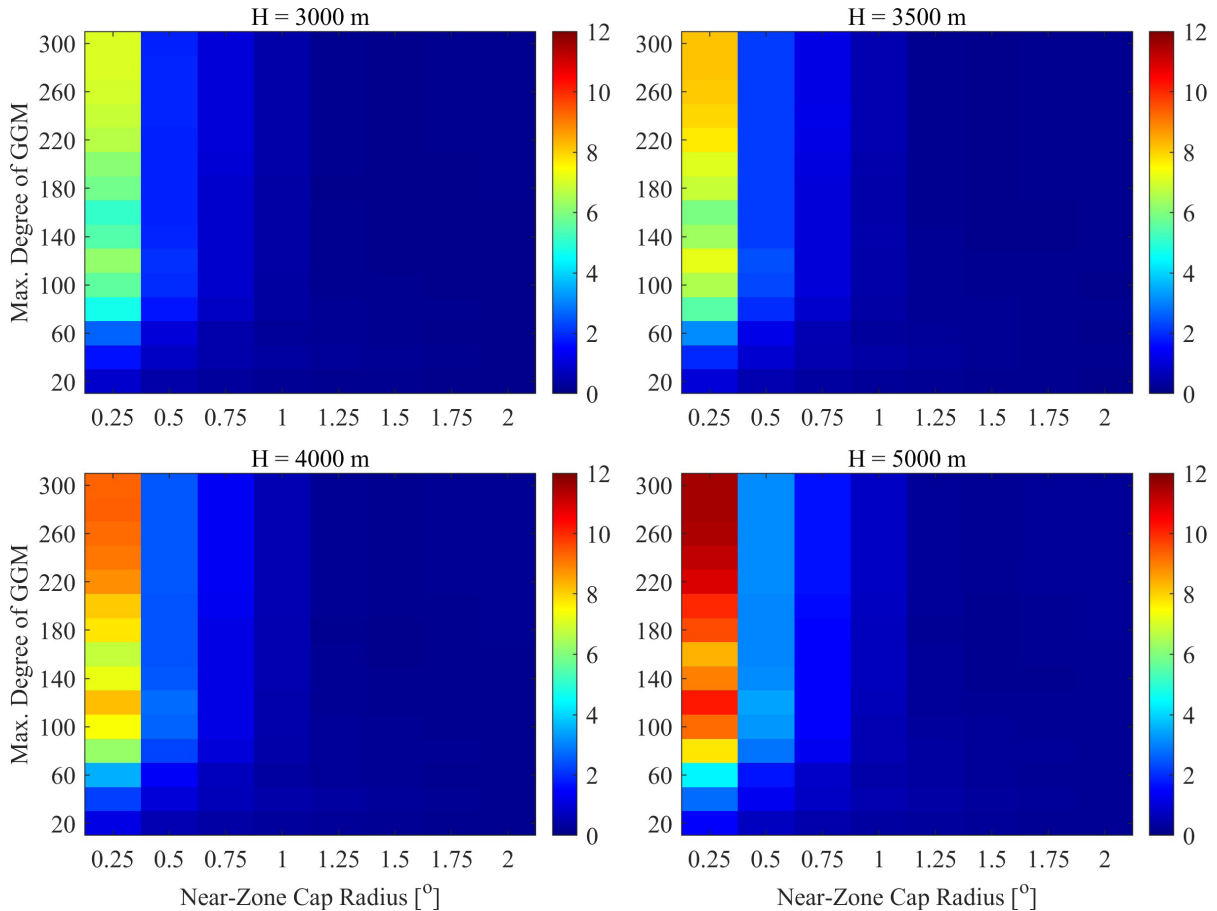
Figure 5. The maximum far-zone effects in the study region depending on the near-zone cap size radius, maximum degree of GGM, and upward continuation height levels. Units are in mGal.

Table 2. Descriptive statistics of the differences between Poisson upward continued gravity anomaly (Δg) data and their synthetic counterparts obtained from ultrahigh-resolution xGM2019e model. #1: Unreduced Δg on the geoid surface, #2: Unreduced Δg on the Earth's surface, #3: GGM[ES] Reduced, #4 Spherical Bouguer Reduced, #5: GGM[GS] + Spherical Bouguer Reduced, #6: GGM[ES] + RTM Reduced, #7: GGM[GS] + DTE (Helmert 2nd Cond.) Reduced. Units are in mGal. (S: Standard Poisson Kernel, M: Modified Poisson Kernel).

| Upward cont. height level | Input data to Poisson Integral: | #1 | #2 | #3 | #4 | #5 | #6 | #7 |
	Poisson kernel applied:	S	S	M	S	M	M	M
3000 m above the geoid surface	Min:	−0.31	−73.15	−69.31	0.75	1.03	−9.28	−36.73
	Max:	0.09	5.20	10.09	37.08	37.68	26.60	10.27
	Mean:	**−0.13**	−5.50	−3.64	6.63	7.49	**0.75**	0.71
	Std:	**0.04**	8.49	7.88	3.93	3.88	**2.37**	5.01
3500 m above the geoid surface	Min:	−0.34	−63.32	−59.91	0.98	1.21	−5.88	−30.62
	Max:	0.04	2.69	7.53	25.27	25.97	14.66	9.51
	Mean:	**−0.15**	−5.48	−3.64	6.75	7.75	**0.74**	0.70
	Std:	**0.05**	7.57	7.00	3.59	3.54	**1.79**	4.44
4000 m above the geoid surface	Min:	−0.39	−55.32	−52.33	1.12	1.39	−3.81	−30.62
	Max:	0.00	1.38	6.21	18.97	19.77	8.41	9.51
	Mean:	**−0.17**	−5.46	−3.63	6.86	8.01	**0.72**	0.70
	Std:	**0.05**	6.83	6.32	3.42	3.37	**1.48**	4.44
5000 m above the geoid surface	Min:	−0.48	−43.33	−41.11	1.41	1.65	−2.44	−22.12
	Max:	−0.05	−0.27	5.10	13.40	15.34	5.32	7.90
	Mean:	**−0.22**	−5.41	−3.60	7.07	8.50	**0.68**	0.66
	Std:	**0.06**	5.74	5.36	3.24	3.23	**1.20**	3.59

On the other hand, the original unreduced synthetic ground gravity field data (for example, see Figure 2b for gravity anomaly) upward-continued to the same exterior height levels produce the worst comparison results. The second data columns (#2) of Tables 2 and 3 present similar descriptive statistics to that in case #1. Figure 6 shows the spatial variations of differences between Poisson upward-continued unreduced ground gravity anomaly data and its synthetic counterpart. If the ground anomalous data is to be input directly in the Poisson integral without any reduction applied, then the upward values is systematically biased with a mean of about 5.5 mGal in our experiment.

Maximum differences are observed particularly above the rugged terrains on the central part. The differences for the lowest continuation height level can reach up to 73

mGal, while they are close to zero above the flat parts of the study region, especially directly above the sea surface. Not surprisingly, it can easily be inferred from the results that the higher the upward continuation height level, the lower and better the statistics and variability we have. We can conclude that long- and short-wavelength gravity signals must be accounted for when upward continuing the ground anomalous gravity field data.

4.3. Upward continuation of reduced ground gravity field data
Several combinations of long- and short-wavelength reductions have been applied to the ground gravity field data, used as input to the evaluation of the Poisson integral, to produce various solutions for comparison purposes.
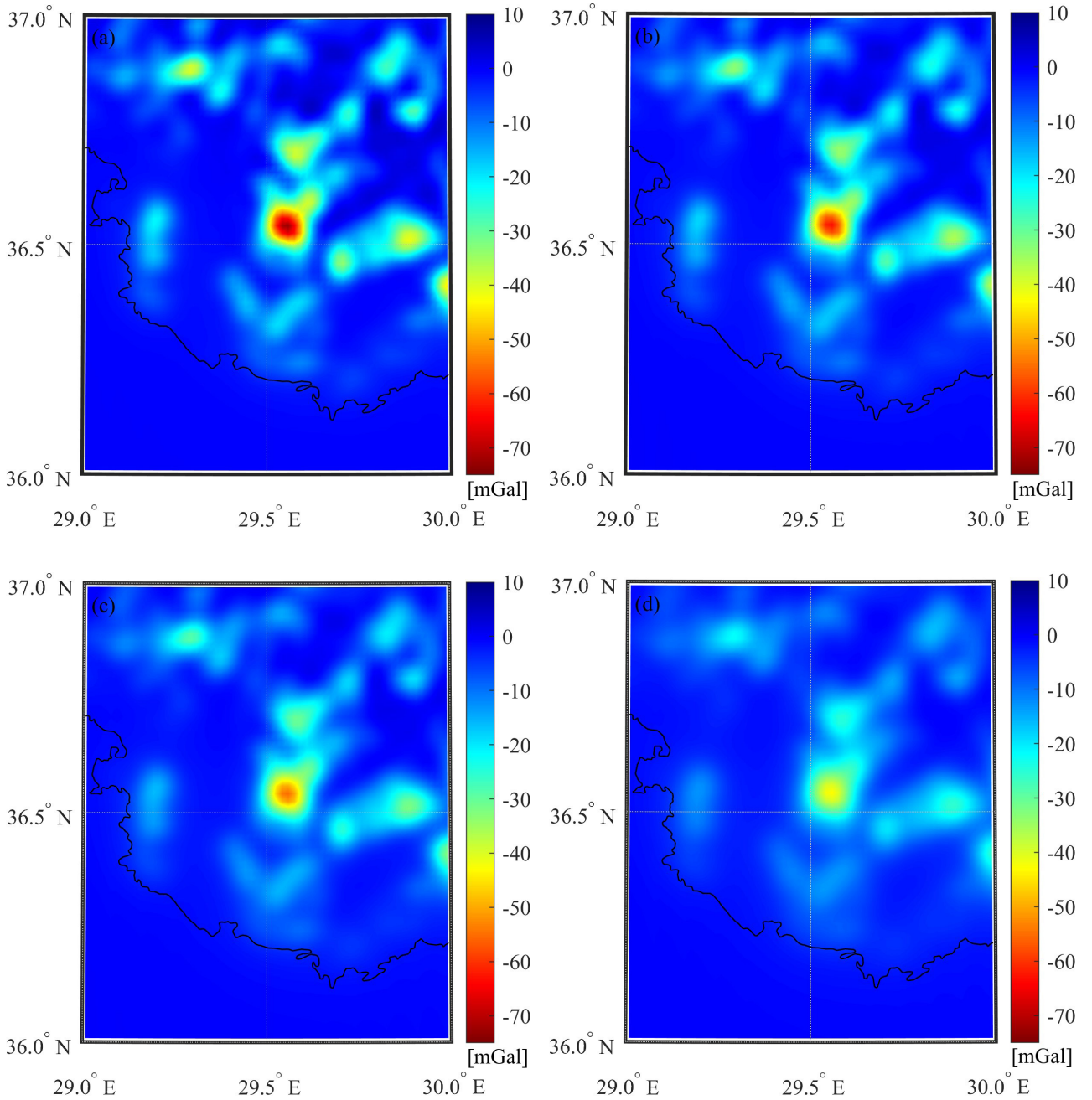
Figure 6. Spatial distribution of the differences between Poisson upward continued unreduced ground gravity anomaly data and its synthetic counterpart (see the data column #2 of Table 2). (a) 3000 m above the geoid, (b) 3500 m above the geoid, (c) 4000 m above the geoid, (d) 5000 m above the geoid. Units are in mGal.

In the first analysis, we have reduced the input ground anomalous data only for long-wavelength effects computed on the Earth's surface (ES), i.e., GGM^{ES} term in Tables 2 and 3. We have then upward continued the reduced or residual data to the corresponding height levels, restored the removed effects at the new levels, and compared the solutions with the synthetic gravity field data. The

GOCO06s satellite-only GGM has been used to compute the removed and restored long-wavelength gravity field signals. Several options for the maximum degree of GGM have been evaluated, (e.g., $n_{max}^{GOCO06S} \in$ [20, 40, 60, ..., 260, 280, 300]), but the best results are obtained with $n_{max}^{GOCO06S} =$ 300. We have also employed both the standard and modified spheroidal Poisson kernels (see

Section 2.3. The statistics of the differences are presented Tables 1 and 2 (see the data column #3). Although the contribution of long-wavelength remove-restore procedure is not clearly distinguishable with those of the unreduced ground data (see the data column #2 in Tables 2 and 3), the implementation can merely reduce the mean bias and the standard deviation, but the range between the extreme values stays similar. It should also be noted that the differences between the statistics are negligible when standard or modified Poisson kernel is applied. It is evident that the sole long-wavelength reduction is not adequate when upward continuing the ground gravity anomaly or disturbance data over the rugged terrain.

In the second and third analyses, we have employed spherical Bouguer topographic reduction. The spherical terrain effect on gravity from mean sea level to Earth's surface has been computed at the locations of near-zone ground points for reduction purposes and at the locations of upward continuation points for restoring purposes by numerically integrating the Eq. (18) using constant density of 2670 kgm^{-3}. To reduce computational costs, cascading grid resolutions of DEM data have been utilized with 3" × 3" in the close proximity of a computation point up to an extension of 1.5° and coarser resolution of 15' × 15' for the remainder to the full globe. We have first reduced the ground anomalous gravity field data only by spherical Bouguer effect and performed the upward continuation. While Tables 2 and 3 present the statistics of the comparisons (see the data column #4), Figure 7 displays the spatial distributions of the differences regarding the gravity anomalies. There is no doubt that the application of spherical Bouguer reduction improves the agreement remarkably. The main variability measures such as range and standard deviation reduce by an amount of approximately 50% when compared with those of the unreduced data. While the minimum values are observed above the sea and low-lying coastal areas, the maximums are spotted on relatively higher central and northeast part of the study area. However, the implementation results in positively biased solutions with a mean of about 7 mGal despite the restoring process. This can be attributed to the indirect effect introduced by the removal of the full topographic effect which causes the gravity field to change due to the mass shifting. The inclusion of the long-wavelength reduction computed on the geoid surface (GS), i.e., GGM^{GS} term in Tables 2 and 3, does not contribute to the former solutions. We have added the related statistics in Tables 2 and 3 (see the data column #5) for the sake of completeness.

We have tested the GGM^{ES} plus RTM mass reduction scheme in our fourth analysis. For this, we computed the GGM^{ES} from GOCO06s up to maximum d/o 300, i.e., $n_{max}^{GOCO06S} = 300$. Subsequently, the reference topography

surface has been built using DTM2006.0 model again up to maximum d/o 300. Finally, the RTM effect on gravity has been calculated by numerically integrating the Eq. (18) similar to the derivation of the spherical Bouguer effect, but this time, the lower limit of the innermost integration has been set to $r_1 = R + Href(\Omega')$. The ground anomalous gravity field data on the Earth's surface within the near-zone have been reduced by GGM^{ES} plus RTM, then upward continued to exterior height levels, and the removed effects have been restored at the computation points. Comparisons with the synthetic data exhibit the best agreement of all the reduction schemes we have evaluated so far. The data column #6 in Tables 2 and 3 present the comparison statistics and Figure 8 shows the spatial distribution of the differences. The mean biases are now reduced below 1 mGal level with standard deviations of around 1-2 mGal.

The last mass reduction scheme evaluated in the study is Helmert's second method of condensation. Contrary to the spherical Bouguer reduction which removes all terrain masses above the mean sea level, this model principally replaces the Earth's topographical masses with an infinitesimal condensation layer on the geoid. This results in the generation of a new gravity field that closely resembles the original field. Therefore, the indirect effect stemming from the change in the gravity field is supposed to be smaller in this reduction scheme compared to spherical Bouguer. To use this model, the real field quantities have been first transformed into corresponding quantities in Helmert space which requires the derivation of DTE expressed in Eq. (19). We have followed the similar computational methodology already applied for the spherical Bouguer and RTM calculations in evaluating Eq. (18). The so-called Helmertised ground gravity anomaly and disturbance data also reduced for the long-wavelength effects have upward continued and compared with the synthetic data. The last data column #7 in Tables 2 and 3 presents the comparison statistics. It is no surprise that the mean biases between the Poisson upward continued and the synthetic reference are the smallest we have obtained so far due to the modest indirect effect, but the variability measures are higher than those of spherical Bouguer and RTM reductions.

We have also attempted to figure out whether the variability or smoothness of the ground gravity field as well as its correlation with topographic variations is related with the obtained upward continuation results. Table 4 presents the variability of the input data used in the discrete Poisson upward integral in terms of standard deviation and its correlation with point heights. The unreduced gravity anomaly or gravity disturbance data on the geoid surface possesses the highest variability and has the strongest positive correlation with topographic variations among
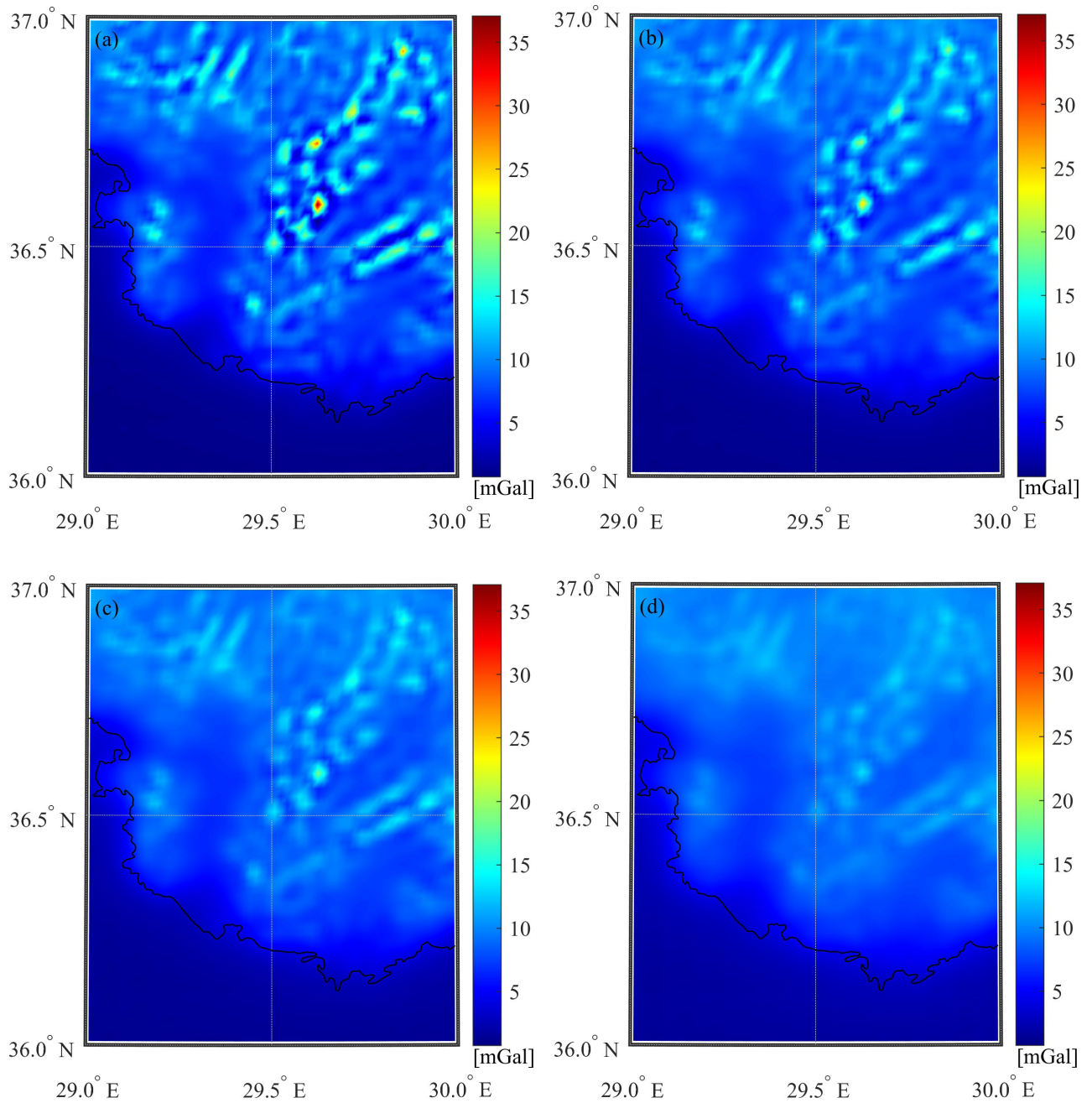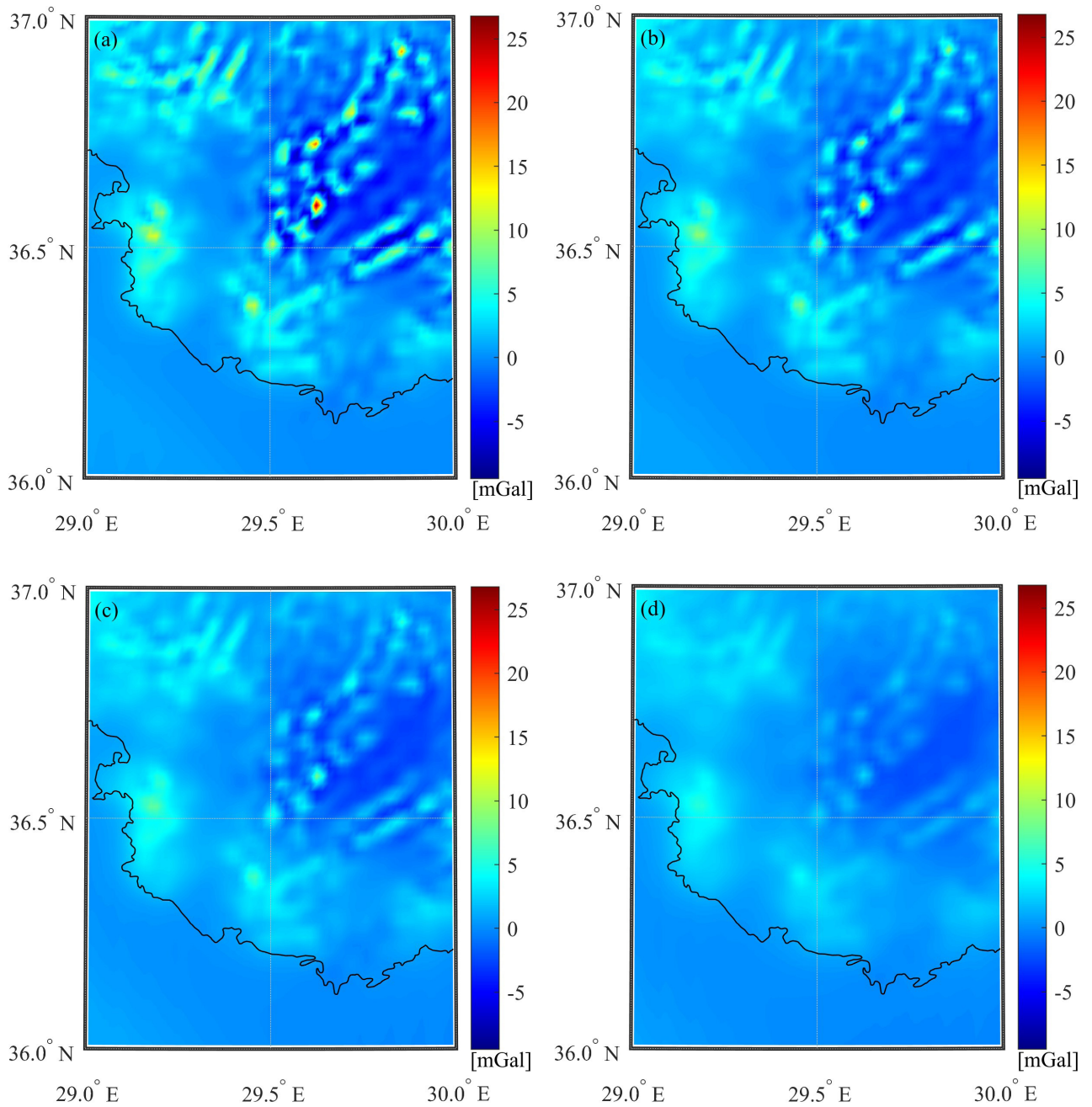
Figure 7. Spatial distribution of the differences between Poisson upward continued reduced-restored ground gravity anomaly by spherical Bouguer and its synthetic counterpart (see the data column #4 of Table 2). (a) 3000 m above the geoid, (b) 3500 m above the geoid, (c) 4000 m above the geoid, (d) 5000 m above the geoid. Units are in mGal.

the other input datasets, but the upward continued version of this data gives the best agreement with the synthetic data. While the GGM[ES] reduced data (see data column #3) or GGM[GS] + DTE reduced data (see data column #7) has the least variability and relatively lower correlation with topography, their upward continued versions are not compatible with GGM[ES] + RTM reduced data which has close standard deviation and correlation coefficient to that of unreduced data on the geoid surface. We could not find any evidence that smoothing the variability of input data or eliminating its correlation with topography produce better results.

Figure 8. Spatial distribution of the differences between Poisson upward continued reduced-restored ground gravity anomaly by GGM[ES] plus RTM and its synthetic counterpart (see the data column #6 of Table 2). (a) 3000 m above the geoid, (b) 3500 m above the geoid, (c) 4000 m above the geoid, (d) 5000 m above the geoid. Units are in mGal.

5. Summary and conclusion

Discrete spherical Poisson's upward continuation of ground gravity field data to the exterior continuation levels close to the Earth's surface has been revisited. We have reviewed the theory and literature, then performed experimental investigations in the southwest of Türkiye using synthetic data derived from an ultrahigh-degree GGM and using an in-house software developed in MATLAB environment.

Because the gravity field data are often limited in spatial extent in practice, we have first studied the far-zone effect or truncation error caused by masses outside the data area. It is concluded that the far-zone contribution should be taken into account when the near zone cap size radius is less than 1° for the upward continuation height levels close to the Earth's surface. Should the far-zone effect be incorporated in the upward continuation process,

Table 3. Descriptive statistics of the differences between Poisson upward continued gravity disturbance (δg) data and their synthetic counterparts obtained from ultrahigh-resolution xGM2019e model. #1: Unreduced δg on the geoid surface, #2: Unreduced δg on the Earth's surface, #3: GGM^{ES} Reduced, #4 Spherical Bouguer Reduced, #5: GGM^{GS} + Spherical Bouguer Reduced, #6: GGM^{ES} + RTM Reduced, #7: GGM^{GS} + DTE (Helmert 2nd Cond.) Reduced. Units are in mGal. (S: Standard Poisson Kernel, M: Modified Poisson Kernel).

Upward cont. height level	Input data to poisson integral:	#1	#2	#3	#4	#5	#6	#7
	Poisson kernel applied:	S	S	M	S	M	M	M
3000 m above the geoid surface	Min:	−0.40	−73.39	−69.41	0.56	0.94	−9.31	−36.87
	Max:	−0.01	5.06	10.11	36.88	37.57	26.59	10.25
	Mean:	**−0.22**	−5.62	−3.65	6.51	7.46	**0.74**	0.68
	Std:	**0.04**	8.51	7.89	3.91	3.86	**2.37**	5.02
3500 m above the geoid surface	Min:	−0.45	−63.56	−60.00	0.87	1.21	−5.90	−30.76
	Max:	−0.08	2.53	7.54	25.05	25.87	14.64	9.50
	Mean:	**−0.26**	−5.62	−3.64	6.61	7.73	**0.73**	0.68
	Std:	**0.05**	7.59	7.01	3.57	3.52	**1.79**	4.46
4000 m above the geoid surface	Min:	−0.51	−55.57	−52.41	1.00	1.39	−3.84	−26.97
	Max:	−0.13	1.20	6.23	18.75	19.68	8.39	8.86
	Mean:	**−0.30**	−5.61	−3.63	6.70	7.98	**0.72**	0.66
	Std:	**0.05**	6.85	6.33	3.40	3.36	**1.48**	4.08
5000 m above the geoid surface	Min:	−0.63	−43.59	−41.18	1.25	1.64	−2.46	−22.23
	Max:	−0.21	−0.42	5.11	13.15	15.29	5.31	7.88
	Mean:	**−0.38**	−5.60	−3.61	6.88	8.48	**0.67**	0.63
	Std:	**0.06**	5.76	5.37	3.22	3.21	**1.20**	3.60

Table 4. Variability of the data input to Poisson integral and its correlation with corresponding topographic height. Standard deviations are given in mGal unit.

Data Column Tables 2 and 3	Description	Data Type	Std	Corr. Coeff.
#1	Unreduced data on the geoid surface (Reference data)	Δg	**91.43**	**0.78**
		δg	**94.86**	**0.78**
#2	Unreduced data on the Earth's surface	Δg	87.72	0.76
		δg	91.22	0.76
#3	GGM[ES] reduced data on the Earth's surface	Δg	31.70	0.25
		δg	31.82	0.25
#4	Spherically Bouguer reduced data on the Earth's surface	Δg	58.68	0.13
		δg	61.23	0.17
#5	GGM[GS] + spherically Bouguer reduced data on the Earth's surface	Δg	60.50	−0.86
		δg	60.56	−0.86
#6	GGM[ES] + RTM reduced data on the Earth's surface	Δg	**74.42**	**0.61**
		δg	**77.54**	**0.62**
#7	GGM[GS] + DTE reduced data on the Earth's surface	Δg	30.45	0.29
		δg	30.56	0.29

the maximum degree of the GGM should not be less than 220, 120, and 80 for the cap radii of 0.25°, 0.50°, and below 1°, respectively.

In order to prove the standard theory experimentally and test our in-house software, we have spherically upward continued the anomalous gravity field data given on the geocentric sphere, which approximates the geoid surface, to four exterior height levels and compare the results with their synthetic counterparts. We have found out very good agreement between the upward continued and synthetic datasets, which proves the theory and confirms the effectiveness of the in-house software.

We have finally attempted to upward continue the gravity field data given on the complex and irregular topography of the Earth's surface. We have applied the well-known remove-compute-restore procedure by incorporating many reduction schemes for the long- and short-wavelength effects. Moreover, we have assessed the

contribution of modified Poisson kernel over the standard kernel. Numerical results have showed that the GGM plus the RTM reduction scheme outperforms different combinations of GGM and topographic gravity reductions. Smoothing the variability of input data entered into the Poisson upward continuation integral or eliminating its correlation with topography does not yield better continuation results. It is also shown that the contribution of the modified Poisson kernel is negligible compared to the standard kernel.

Conflict of interest
The authors declare no conflict of interests.

Data availability
The MATLAB functions used in the computations can be shared upon plausible request. Please contact the corresponding author at msimav@msu.edu.tr

References

Alberts B, Klees R (2004). A comparison of methods for the inversion of airborne gravity data. Journal of Geodesy 78: 55-65. https://doi.org/10.1007/s00190-003-0366-x

Blakely RJ (1995). Potential theory in gravity and magnetic applications: Cambridge University Press. https://doi.org/10.1017/CBO9780511549816

Bucha B, Janák J (2014). A MATLAB-based graphical user interface program for computing functionals of the geopotential up to ultra-high degrees and orders: efficient computation at irregular surfaces. Computers & Geosciences 66: 219-227. https://doi.org/10.1016/j.cageo.2014.02.005

Courtillot V, Ducruix J, Le Moüel JL (1978). Inverse methods applied to continuation problems in geophysics. In: Sabatier PC (ed.) Applied Inverse Problems. Berlin: Springer-Verlag, pp. 48–82.

Cruz JY, Laskowski P (1984). Upward continuation of surface gravity anomalies. Reports of the Department of Geodetic Science and Surveying, Report No. 360. The Ohio State University, Columbus, Ohio, USA. https://earthsciences.osu.edu/sites/earthsciences.osu.edu/files/report-360.pdf

D'Urso MG (2013). On the evaluation of the gravity effects of polyhedral bodies and a consistent treatment of related singularities. Journal of Geodesy 87: 239-252. https://doi.org/10.1007/s00190-012-0592-1

Featherstone WE, Evans JD, Olliver JG (1998). A Meissl-modified Vaníček and Kleusberg kernel to reduce the truncation error in gravimetric geoid computations. Journal of Geodesy 72: 154-160. https://doi.org/10.1007/s001900050157

Featherstone WE (2003). Software for computing five existing types of deterministically modified integration kernel for gravimetric geoid determination. Computers & Geosciences 29: 183-193. https://doi.org/10.1016/S0098-3004(02)00074-2

Fedi M, Rapolla A, Russo G (1999). Upward continuation of scattered potential field data. Geophysics 64: 443-451. https://doi.org/10.1190/1.1444549

Forsberg R, Tscherning CC (1981). The use of height data in gravity field approximation by collocation. Journal of Geophysical Research 86 (B9): 7843-7854. https://doi.org/10.1029/JB086iB09p07843

Forsberg R (1984). A study of terrain reductions, density anomalies and geophysical inversion methods in gravity field modeling. Report No. 355, Department of Geodetic Science and Surveying, The Ohio State University, Columbus, USA.

Forsberg R (1998). The use of spectral techniques in gravity field modelling: Trends and perspectives, Physics and Chemistry of the Earth 23 (1): 31-39. https://doi.org/10.1016/S0079-1946(97)00238-3

Grombein T, Seitz K, Heck B (2013). Optimized formulas for the gravitational field of a tesseroid. Journal of Geodesy 87: 645-660. https://doi.org/10.1007/s00190-013-0636-1

Guo Z, Tao C (2020). Potential field continuation in spatial domain: A new kernel function and its numerical scheme. Computers & Geosciences 136. https://doi.org/10.1016/j.cageo.2020.104405

Heiskanen WA, Moritz H (1967). Physical geodesy. San Francisco, CA, USA: W.H. Freeman and Company.

Hinze WJ, von Frese RRB, Saad AH (2013). Gravity and Magnetic Exploration: Principles, Practices and Applications. New York: Cambridge University Press. https://doi.org/10.1017/CBO9780511843129

Huang J (2002). Computational methods for the discrete downward continuation of the earth gravity and effects of lateral topographical mass density variation on gravity and geoid. PhD Thesis, Department of Geodesy and Geomatics Engineering, the University of New Brunswick, Fredericton, Canada.

Hwang C, Hsiao YS, Shih HC, Yang M, Chen KH et al. (2007). Geodetic and geophysical results from a Taiwan airborne gravity survey: data reduction and accuracy assessment. Journal of Geophysical Research Solid Earth 112: B04407. https://doi.org/10.1029/2005JB004220

Jageler AH (1976). Improved hydrocarbon reservoir evaluation through use of borehole-gravimeter data. Journal of Petroleum Technology 28 (6): 709-718. https://doi.org/10.2118/5511-PA

Kern M (2003). An analysis of the combination and downward continuation of satellite, airborne and terrestrial gravity data. PhD, Department of Geomatics Engineering, Calgary, Alberta, Canada.

Kern M, Schwarz KKP, Sneeuw N (2003). A study on the combination of satellite, airborne, and terrestrial gravity data. Journal of Geodesy 77: 217-225. https://doi.org/10.1007/s00190-003-0313-x

Kvas A, Brockmann JM, Krauss S, Schubert T, Gruber T et al. (2021). GOCO06s – a satellite-only global gravity field model. Earth System Science Data 13: 99-118. https://doi.org/10.5194/essd-13-99-2021

Li X, Huang J, Klees R. Forsberg R, Willberg M et al. (2022). Characterization and stabilization of the downward continuation problem for airborne gravity data. Journal of Geodesy 96: 18. https://doi.org/10.1007/s00190-022-01607-y

Martinec Z (1996). Stability investigations of a discrete downward continuation problem for geoid determination in the Canadian Rocky Mountains. Journal of Geodesy 70: 805-828. https://doi.org/10.1007/BF00867158

Moritz H (1980). Advanced physical geodesy. Wichmann Verlag, Karlsruhe.

Nagy D, Papp G, Benedek J (2000). The gravitational potential and its derivatives for the prism. Journal of Geodesy 74: 552-560. https://doi.org/10.1007/s001900000116

Novák P (2000). Evaluation of gravity data for the Stokes-Helmert solution to the geodetic boundary-value problem. Technical Report No. 207, UNB, Fredericton, Canada.

Novák P, Kern M, Schwarz KP, Heck B (2001). The determination of the geoid from airborne gravity data. Tech. Rep. UCGE No. 30013, Department of Geomatics Engineering, Calgary.

Novák P, Heck B (2002). Downward continuation and geoid determination based on band-limited airborne gravity data. Journal of Geodesy 76: 269-278. https://doi.org/10.1007/s00190-002-0252-y

Paul M (1973). A method of evaluation the truncation errors coefficients for geoidal heights. Bulletin Géodésique 110: 413-425. https://doi.org/10.1007/BF02521951

Pavlis NK, Factor JK, Holmes SA (2007). Terrain-related gravimetric quantities computed for the next EGM. In: Proceedings of the 1st International Symposium of the International Gravity Field Service, Harita Dergisi 18: 318-323.

Qu Q, Yu S, Zhu G, Chang X, Zhou M et al. (2021). An upward continuation method based on spherical harmonic analysis and its application in the calibration of satellite gravity gradiometry data, Solid Earth Discuss [preprint], https://doi.org/10.5194/se-2020-201

Sandwell DT, Müller RD, Smith WHF, Garcia E, Francis R (2014) New global marine gravity model from CryoSat-2 and Jason-1 reveals buried tectonic structure. Science 346 (6205): 65-67. https://doi.org/10.1126/science.1258213

Sasagawa GS, Crawford W, Eiken O, Nooner S, Stenvold T et al. (2003) A new sea-floor gravimeter. Geophysics 68 (2): 544-553. https://doi.org/10.1190/1.1567223

Schwartz KP (1978). Geodetic improperly posed problems and their regularization. Lecture Notes of the Second International School of Advanced Geodesy, Erice.

Schwarz KP, Sideris MG, Forsberg R (1990). The use of FFF methods in physical geodesy. Geophysical Journal International 100: 485-514.

Simav M, Becker D, Yildiz H, Hoss M (2020). Impact of temperature stabilization on the strapdown airborne gravimetry: a case study in Central Turkey. Journal of Geodesy 94: 41. https://doi.org/10.1007/s00190-020-01369-5

Simav M, Yıldız H (2021). Quantifying the bathymetric stripping gravity corrections of global seawater and major lakes over Turkey. Turkish Journal of Earth Sciences 30: 916-927. https://doi.org/10.3906/yer-2105-38

Sjöberg LE (1981). Least-squares combination of satellite and terrestrial data in physical geodesy Annales Geophysicae 37: 25-30.

Smith NL (1950). The case for gravity data from boreholes. Geophysics 15 (4): 605-636. https://doi.org/10.1190/1.1437623

Smith DA, Holmes SA, Li X, Guillaume S, Wang YM et al. (2013). Confirming regional 1 cm differential geoid accuracy from airborne gravimetry: the geoid slope validation survey of 2011. Journal of Geodesy 87: 885-907. https://doi.org/10.1007/s00190-013-0653-0

Torge W (1989). Gravimetry. Walter de Gruyter, Berlin.

Tozer B, Sandwell DT, Smith WHF, Olson C, Beale JR et al. (2019). Global bathymetry and topography at 15 arcsec: SRTM15+. Earth and Space Science 6 (10): 1847-1864. https://doi.org/10.1029/2019EA000658

Tsoulis D (2012). Analytical computation of the full gravity tensor of a homogeneous arbitrarily shaped polyhedral source using line integrals. Geophysics 77 (2): F1–F11. https://doi.org/10.1190/geo2010-0334.1

Tziavos IN, Sideris MG (2013). Topographic reductions in gravity and geoid modeling. In: Sansò F and Sideris M. (eds) Geoid Determination. Lecture Notes in Earth System Sciences 110. Springer, Berlin, Heidelberg. https://doi.org/10.1007/978-3-540-74700-0_8

Uieda L, Barbosa VCF, Braitenberg C (2016). Tesseroids: Forward-modeling gravitational fields in spherical coordinates. Geophysics 81 (4): F41-F48. https://doi.org/10.1190/geo2015-0204.1

van Gelderen M, Rummel R (2001). The solution of the general geodetic boundary value problem by least squares. Journal of Geodesy 75: 1-11 https://doi.org/10.1007/s001900000146

Vaníček P, Kleusberg A (1987). The Canadian geoid – Stokesian approach. Manuscripta Geodaetica 12: 86–98.

Vaníček P, Martinec Z (1994). The Stokes-Helmert scheme for the evaluation of a precise geoid. Manuscripta Geodaetica 19: 119-128.

Vaníček P, Sun W, Ong P, Martinec Z, Najafi M et al. (1996). Downward continuation of Helmert's gravity. Journal of Geodesy 71: 21-34. https://doi.org/10.1007/s001900050072

Vaníček P, Tenzer R, Sjöberg LE, Martinec Z, Featherstone WE (2004). New view of the spherical Bouguer gravity anomaly. Geophysical Journal International 159 (2): 460-472. https://doi.org/10.1111/j.1365-246X.2004.02435.x

Vaníček P, Kingdon R (2015). Gravimetry. Reference Module in Earth Systems and Environmental Sciences, Elsevier. https://doi.org/10.1016/B978-0-12-409548-9.09145-4.

Wild Pfeiffer F (2008). A comparison of different mass elements for use in gravity gradiometry. Journal of Geodesy 82: 637-653. https://doi.org/10.1007/s00190-008-0219-8

Willberg M, Zingerle P, Pail R (2020). Integration of airborne gravimetry data filtering into residual least-squares collocation: example from the 1 cm geoid experiment. Journal of Geodesy 94: 75. https://doi.org/10.1007/s00190-020-01396-2

Wong L, Gore R (1969). Accuracy of geoid heights from modified Stokes kernels. Geophysical journal of the Royal Astronomical Society 18: 81-91. https://doi.org/10.1111/j.1365-246X.1969.tb00264.x

Yamazaki D, Ikeshima D, Tawatari R, Yamaguchi T, O'Loughlin F et al. (2017). A high accuracy map of global terrain elevations. Geophysical Research Letters 44 (11): 5844-5853. https://doi.org/10.1002/2017GL072874

Yildiz H, Forsberg R, Tscherning CC, Steinhage D, Eagles G et al. (2017). Upward continuation of Dome-C airborne gravity and comparison with GOCE gradients at orbit altitude in east Antarctica. Studia Geophysica et Geodaetica 61: 53-68. https://doi.org/10.1007/s11200-015-0634-2

Zingerle P, Pail R, Gruber T, Oikonomidou X (2020). The combined global gravity field model XGM2019e. Journal of Geodesy 94: 66. https://doi.org/10.1007/s00190-020-01398-0